

# Atomically flat single-crystalline gold nanostructures for plasmonic nanocircuitry

Jer-Shing Huang<sup>1,\*</sup>, Victor Callegari<sup>3</sup>, Peter Geisler<sup>1</sup>, Christoph Brüning<sup>1</sup>, Johannes Kern<sup>1</sup>, Jord C. Prangsma<sup>1</sup>, Pia Weinmann<sup>2</sup>, Martin Kamp<sup>2</sup>, Alfred Forchel<sup>2</sup>, Paolo Biagioni<sup>4</sup>, Urs Sennhauser<sup>3</sup> & Bert Hecht<sup>1,†</sup>

<sup>1</sup>*Nano-Optics & Biophotonics Group, Experimentelle Physik 5, Physikalisches Institut, Wilhelm-Conrad-Röntgen-Center for Complex Material Systems, Universität Würzburg, Am Hubland, D-97074 Würzburg, Germany*

<sup>2</sup>*Technische Physik, Physikalisches Institut, Wilhelm-Conrad-Röntgen-Center for Complex Material Systems, Universität Würzburg, Am Hubland, D-97074 Würzburg, Germany*

<sup>3</sup> *EMPA, Swiss Federal Laboratories for Materials Testing and Research, Electronics/Metrology/Reliability Laboratory, Ueberlandstrasse 129, CH-8600 Dübendorf, Switzerland*

<sup>4</sup>*CNISM - Dipartimento di Fisica, Politecnico di Milano, Piazza Leonardo da Vinci 32, 20133 Milano, Italy*

\* To whom correspondence should be addressed: [jhaung@physik.uni-wuerzburg.de](mailto:jhaung@physik.uni-wuerzburg.de)

† To whom correspondence should be addressed: [hecht@physik.uni-wuerzburg.de](mailto:hecht@physik.uni-wuerzburg.de)

**Deep subwavelength integration of high-definition plasmonic nanostructures is of key importance for the development of future optical nanocircuitry for high-speed communication, quantum computation and lab-on-a-chip applications. So far the experimental realization of proposed extended plasmonic networks consisting of multiple functional elements remains challenging, mainly due to the multi-crystallinity of commonly used thermally evaporated gold layers. Resulting structural imperfections in individual circuit elements will drastically reduce the yield of functional integrated nanocircuits. Here we demonstrate the use of very large ( $>100\ \mu\text{m}^2$ ) but thin ( $<80\ \text{nm}$ ) chemically grown single-crystalline gold flakes, which, after immobilization, serve as an ideal basis for focused-ion beam milling and other top-down nanofabrication techniques on any desired substrate. Using this methodology we obtain high-definition ultrasmooth gold nanostructures with superior optical properties and reproducible nano-sized features over micrometer length scales. Our approach overcomes the current fabrication bottleneck and opens the road for the realization of extended plasmonic circuitry.**

## **Introduction**

The recent years have seen tremendous activity in the development of basic building blocks of optical nanocircuitry and improved photovoltaic devices which take advantage of plasmonic resonances of noble metals and the associated strongly enhanced local fields [1-4]. Sub-wavelength plasmonic waveguides [5,6], optical nanoantennas [7,8], as well as various plasmonic modulators [9,10] and resonators for ultra sensing and microscopy [8, 11-14] have been suggested and realized experimentally. Furthermore, the strongly enhanced local fields associated with plasmon resonances have been exploited to boost various nonlinear optical phenomena [15,16]. Recently, first steps have been taken to transfer concepts of quantum optics to plasmonics [17-20]. In combination with coherent control techniques for near-field manipulation [21-23], gain materials for field amplification [24-27] and the impedance matching concept for building up optical nanocircuitry [28,29], functional plasmonic nanocircuitry operating at optical frequencies is about to become a field of major scientific and technological impact.

However, when it comes to advanced functional - and therefore necessarily more complex - plasmonic structures, theoretical studies using numerical simulations are far ahead of what is currently in reach of state-of-the-art micro- and nanofabrication techniques. This trend roots in the very small fabrication tolerances that are necessary to yield a desired functionality. Small enough tolerances, however, are very difficult to obtain due to the multi-crystalline structure of thin gold films produced by thermal evaporation [30]. As an illustration we consider a plasmonic transmission line consisting of two wires separated by a nanometer sized gap extending of micrometer distances. While such transmission lines perform well in simulations, in a real structure, fabricated by state-of-the-art nanofabrication techniques, already a single nanometer-scale defect in the gap can lead to a strong power reflection due to the local impedance change and render the structure useless. As a general rule, fabrication tolerances become more critical as the degree of field confinement and enhancement in plasmonic nanostructures increases. For isolated nanostructures with a single critical dimension, such as the feedgap of a

nanoantenna, insufficient fabrication tolerances can be compensated by producing large arrays of similar structures and selecting individuals that match the specification. This approach, however, breaks down as soon as several nanostructures, each with their own critical dimensions, need to be combined in a complex device because the yield of functional devices then decreases rapidly with the number of elements. In addition there is clear evidence that in multi-crystalline nanostructures scattering of plasmons is enhanced [30-32], which has negative consequences for both propagation effects and the achievable maximal near-field intensity enhancement. For the progress of nanoplasmonics, it is, therefore crucial to have methods at hand that allow precise fabrication of complex, functional, single-crystalline plasmonic nanostructures and extended networks.

When applied to the task of manufacturing complex plasmonic nanostructures, electron beam lithography (EBL), the currently most popular fabrication method, suffers from the multi-crystalline character of gold layers and ensuing imperfections introduced by the lift-off process [30, 33]. Moreover, in order to enhance the sticking of very small gold nanostructures to various substrates, including ITO-coated substrates providing DC conductivity, a standard method is to deposit a thin adhesion layer, such as 5 nm of titanium or chromium. This adhesion layer, unfortunately, damps the local plasmonic resonance drastically and, therefore, reduces the plasmon propagation length and near-field intensity enhancement [34-37]. To avoid the adhesion layer, Mühlischlegel et al. [7] have chosen an approach combining EBL and focused-ion beam (FIB) milling to fabricate optical nanoantennas. They first use EBL to fabricate marker structures and large gold patches ( $>1 \mu\text{m}^2$ ), which, during the lift-off, stay firmly attached to the substrate even without adhesion layer. Subsequent FIB milling then yields the desired structures. Using this approach, white light continuum generation with very low excitation powers (down to  $20 \mu\text{W}$ ) has been observed for some of the antennas nominally in resonance with the excitation. Since the gold film produced by vapour deposition consists of randomly oriented crystal grains, the precision of the fabricated structures is limited by the size of the grains due to the fact that different crystal domains show different resistance to FIB milling [33]. The typical diameter of crystal grains in thin layers of vapour-deposited gold is about 30 nm to 50 nm (see Fig. 1c), which impedes the fabrication of structures containing features of comparable size and introduces an intrinsic surface roughness for larger structures which leads to scattering [31] and increased dephasing of surface plasmons. Alternative fabrication methods such as template stripping employing a patterned silicon substrate [38] or induced-deposition mask lithography (IDML) [14] retain the problem of multicrystallinity and therefore cannot effectively remove the nanofabrication bottle neck in plasmonics.

As a new paradigm for the fabrication of extended functional plasmonic nanostructures, we propose using chemically synthesized single-crystalline gold flakes [39-41] (Fig. 1) which are deposited on a substrate and subsequently structured by FIB milling. Using this combination of bottom-up and top-down nanofabrication, we have obtained isolated nanoantennas and more complex plasmonic nanostructures for optical nanocircuitry with superior optical quality, well-defined dimensions, crystallographic orientation, as well as atomically flat

surfaces. The use of chemically synthesized single-crystalline metal flakes is inexpensive, applicable to all kinds of substrate and not limited to gold.

## Methods

The growth of large gold flakes is achieved following the procedure described in ref. 40. As shown in Fig. 1a, the single-crystalline flakes appear as triangles and truncated triangles. The high surface quality of single-crystalline flakes (Fig. 1b) is confirmed by both very low surface roughness ( $<1$  nm) over a large area ( $1 \mu\text{m}^2$ ) as determined by atomic force microscopy and the complete absence of a TPPL signal (Fig. S3 and Fig. S4, Supplementary Information), which is expected to be greatly enhanced by surface roughness [42]. To obtain thin flakes (thickness  $< 80$  nm) with large surface area ( $> 100 \mu\text{m}^2$ ), the reaction temperature has been reduced to  $60^\circ\text{C}$  (Fig. S2, Supplementary Information). Single-crystalline gold flakes are then drop-casted onto ITO coated cover glasses, on which multi-crystalline gold marker-structures with 30 nm thickness are pre-fabricated by EBL. The marker structures can be easily observed in both conventional optical microscopy and scanning electron microscopy (SEM) and therefore facilitating the precise localization and identification of the same gold flakes using both methods. In addition, vapour-deposited markers provide multi-crystalline films for control experiments. Isolated gold flakes of sufficiently large size and spatially homogeneous optical transmission are pre-selected by optical microscopy. Selected flakes are then imaged by SEM to confirm good contact to the substrate and the absence of defects. FIB milling (Helios Nanolab, FEI Company) is applied to single-crystalline flakes that pass all of these criteria as well as to the nearby multi-crystalline marker structures serving as a reference. Best structuring results are obtained for 30 kV acceleration voltage and 1.5 pA Ga-ion current. The degree of near-field intensity enhancement achieved for various single- and multi-crystalline gold nanostructures is characterized using two-photon photoluminescence confocal microscopy (see Supplementary Information for experiment details).

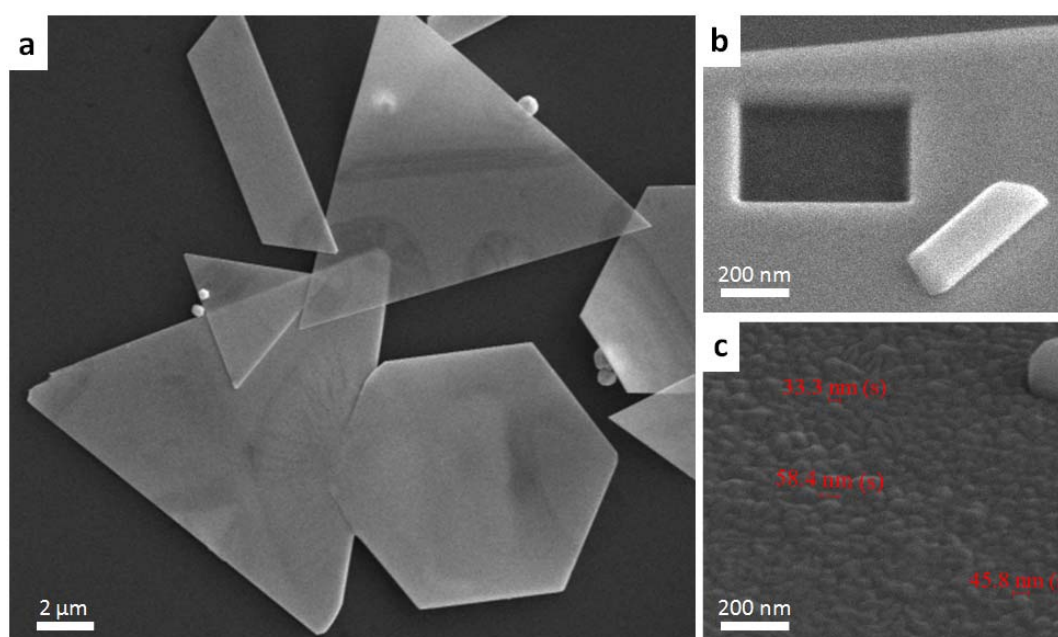


**Figure 1 | SEM images of chemically synthesized gold flakes and the vapour-deposited gold film. (a)**

Overview of a cluster of self-assembled single-crystalline gold flakes. The thickness of the flakes usually varies between 40 nm and 80 nm, but is homogeneous for each flake. (b) Zoomed-in SEM image of the surface of a single-crystalline flake with rectangular area milled by FIB. The nearby particle is a nanoparticle from the suspension. (c) Zoomed-in SEM image of a typical surface of vapor-deposited multi-crystalline gold film (marker structure) consisting of randomly orientated grains (30 – 50 nm) on top of an ITO substrate. Note that (b) and (c) are recorded with 52° tilt angle.

## Results and Discussion

Compared to single-crystalline gold layers prepared by the Czochralski process and subsequent polishing [31,43] or the epitaxial growths of gold layers on lattice-matched substrates, such as mica or MgO, the method proposed here using chemically synthesized gold flakes is easier, cheaper, and requires no specialized instrumentation while the freedom of choosing a substrate at will is retained. The obtained metal layers have minimal surface roughness ( $< 1$  nm over  $1\ \mu\text{m}^2$ , see Supplementary Information) and well-defined crystal orientation [39-41]. As a result, we are able to fabricate nanostructures that exhibit ultrasmooth surfaces and small gaps over extended distances, which is not possible using any other approach. In addition, nanostructures can be fabricated with distinct crystal orientations determined by the orientation of the FIB milling pattern with respect to the single-crystalline gold flake. In Fig. 2a-c we compare the quality of nanostructures fabricated from single-crystalline gold flakes (right) and from vapour-deposited multi-crystalline gold layers of the same thickness (left) fabricated using the same FIB milling pattern and optimized conditions. It is evident that nanostructures with very fine features that extend over large areas can be easily fabricated in the single-crystalline gold flakes. Although for multi-crystalline structures similar structural details (e.g. wire separation) can be achieved, the presence of grains leads to crucial but unpredictable structural defects, such as particles bridging the gap in Fig. 2a and Fig. 2b. The high quality of the structures is reproducible and greatly improved compared to previously used structures [see for example refs. 8,15,30&38]. In contrast to structures fabricated using vapour-deposited multi-crystalline gold films, the quality of plasmonic nanostructures obtained by our new method is largely independent of the surface roughness of ITO substrate (compare Fig. 2a and Fig. 2b for effect of different ITO substrates).

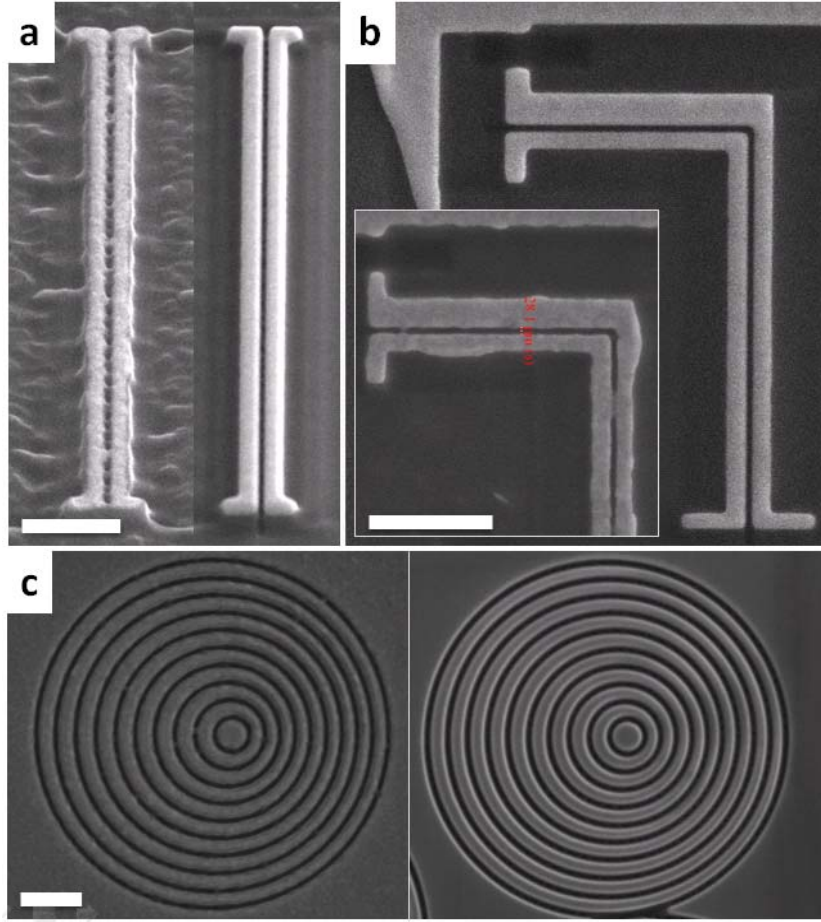


**Figure 2 | SEM images of single- and multi-crystalline gold nanostructures.** (a) Prototype optical nanocircuits (refs. 22,29) fabricated using FIB on a vapor-deposited multi-crystalline (left) and a single-crystalline gold flake deposited on a dip-coated ITO substrate. The length of nanoantennas and the two-wire transmission line are 380 nm and 4  $\mu\text{m}$ , respectively. Note that images in (a) are recorded with 52° tilt angle. (b) Optical nanocircuits with a 90° corner fabricated with FIB on multi-crystalline gold film (inset) and a single-crystalline gold flake on top of sputtered ITO substrate. (c) Asymmetric bull's eye (annular resonator) nanostructure fabricated with FIB on single- and multi-crystalline gold film. All scale bars are 500 nm. Note the increased roughness and structural imperfections of the multi-crystalline structures.

In the following we show that our methods not only improves the structural quality but also the optical properties by reducing the scattering of surface plasmons, similar to improvements observed for single-crystalline silver wires [32] and gold structures [31,43]. Fig. 3a shows an SEM image of bowtie antennas fabricated side-by-side on a single-crystalline gold flake and on a multi-crystalline gold patch prepared by EBL. Note that a 5 nm thick titanium adhesion layer is used here for the multi-crystalline gold film representing the commonly used metal film in EBL.

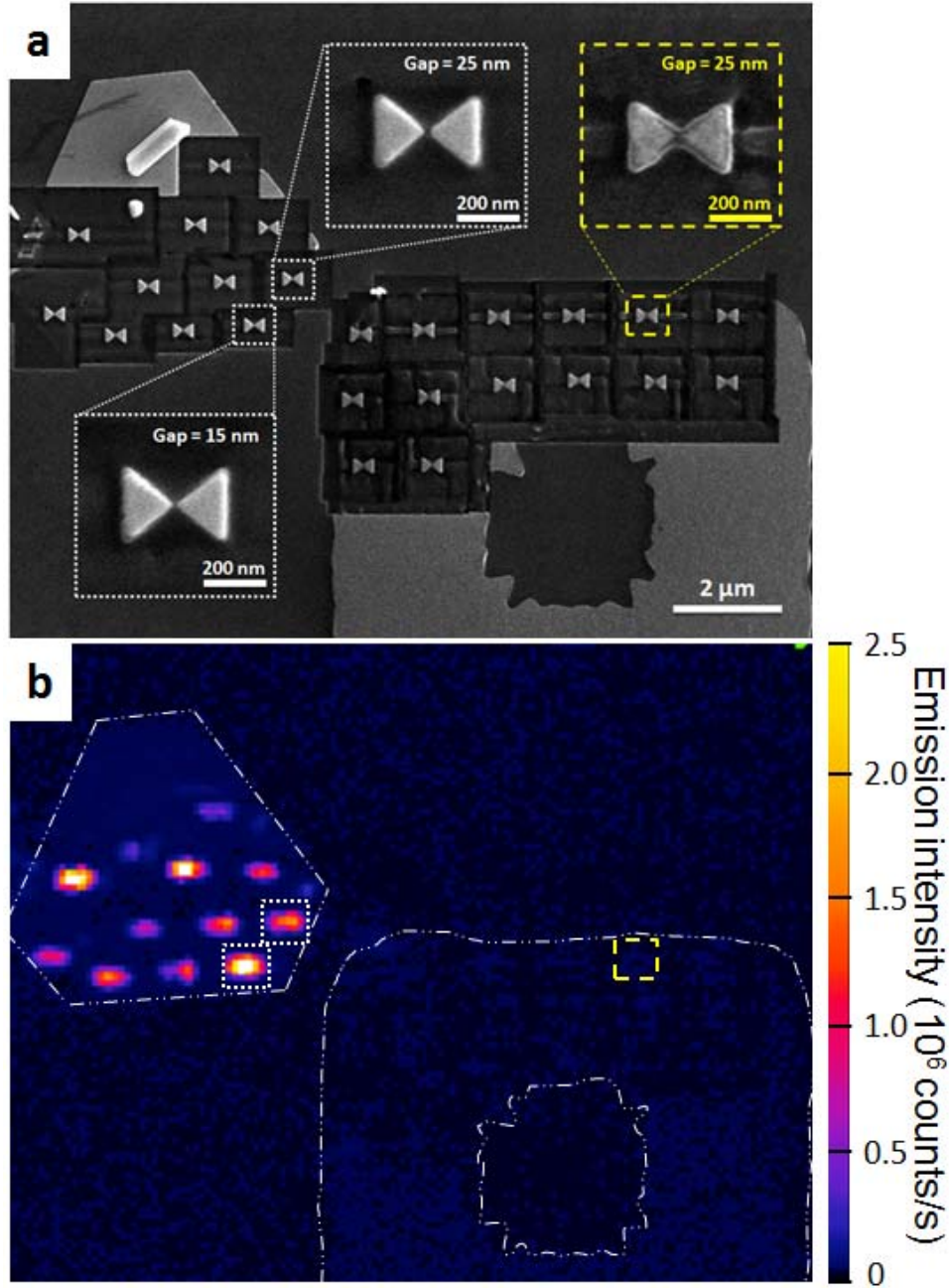


**Figure 3 | SEM image and corresponding TPPL map of single-crystalline and multi-crystalline gold bowtie nanoantennas** (a) SEM image of bowtie antennas fabricated by FIB using a self-assembled single-crystalline gold flake and a vapor-deposited multi-crystalline gold film with 5 nm titanium adhesion layer on top of a sputtered ITO substrate. (b) Map of visible TPPL of the same area shown in (a), obtained by scanning the sample over the tightly focused laser spot ( $\lambda = 830$  nm, NA = 1.4, average power = 70  $\mu$ W, pulse duration = 1 ps ) and recording the emission intensity with a notch filter (O.D. > 6 at 830 nm) and a bandpass filter (frequency window= 450 - 750 nm).

We probe the quality of plasmonic nanostructures by recording their two-photon excited photoluminescence (TPPL, see ref. 44 and Supplementary Information for experiment details). Previous experiments have shown, that the TPPL signal is proportional to  $I^2$  [42,45], where  $I$  is the local near-field intensity enhancement. The recorded TPPL map (Fig. 3b) shows that in addition to the distinct improvement of the structural quality, the single-crystalline antennas show a much higher TPPL



emission count rate ( $>100$  times) upon resonant excitation, indicating much larger field enhancement. The much lower TPPL signal of the multi-crystalline antennas is attributed to the increased damping and slight resonance shift due to the adhesion layer as well as due to enhanced plasmon scattering in the multi-crystalline gold [31]. Besides, since typical materials used for adhesion layers, i.e. Ti and Cr, have higher resistance to FIB milling [33], the minimal ion dose optimized for finest spatial resolution can be insufficient to completely remove the adhesion layer in the gap. Consequently, the impedance and optical properties of the nanoantennas can be strongly influenced due to the remaining material in the gap, which acts as a nanoload [28,46]. For the multi-crystalline bowtie antennas in Fig. 3, the excitation power has to be increased to  $170\text{ }\mu\text{W}$  to obtain a measurable TPPL signal. This is attributed to the fact that, according to numerical simulations, the source excitation spectrum (centered at  $830\text{ nm}$ ) does not exactly hit but only overlaps partially with the broad resonance peak of the bowtie antennas (Fig. S7, Supplementary Information). Any scattering or damping of the near-field reduces the TPPL signal drastically due to the quadratic dependence of TPPL on the integrated intensity in the gold.

We have further slightly varied the gap size of the single-crystalline bowtie antennas. As shown in the inset of Fig. 3, the single-crystalline bowtie antennas with smaller gap ( $15\text{ nm}$ ) show higher TPPL signal than antennas with a larger gap ( $25\text{ nm}$ ) due to the larger near-field intensity enhancement. Deterministically decreasing the gap size to enhance the TPPL signal is only possible for the single-crystalline structures whereas the gap size of the multi-crystalline bowtie antennas is determined by the typical grain size and exhibits a random distribution from  $25$  to  $50\text{ nm}$  when using an optimal ion beam condition.

In order to disentangle the damping introduced by the adhesion layer and the damping due to increased scattering at crystal domain boundaries, we have also prepared multi-crystalline gold patches without adhesion layer using EBL. The SEM image, Fig. 4a, shows linear dipole antenna arrays fabricated using both a single-crystalline gold flake and the multi-crystalline gold film (marked with white-dashed rectangle, 4 rows each containing antennas with the same dimensions). Upon longitudinally polarized illumination with a fixed wavelength of  $830\text{ nm}$  ( $1\text{ ps}$ ,  $50\text{ }\mu\text{W}$ ), now both single- and multi-crystalline antenna arrays exhibit easily detectable TPPL emission. Furthermore, due to the fact that the antenna length is increasing in steps of  $20\text{ nm}$ , from left to right in the arrays ( $196\text{ nm}$  to  $396\text{ nm}$ , respectively), a dependence of the TPPL emission rate on the antenna length is observed (Fig. 4b-c), which reaches a maximum for those antennas whose resonance has the best spectral overlap with the excitation source. A second maximum related to the antibonding mode [44] is also seen. We observe that on average, the single-crystalline antennas show much higher emission count rates even though the structural parameters of most single- and multi-crystalline antenna pairs are nearly identical. In addition to the higher count rate, the single-crystalline antenna array much better reproduces the length-dependent resonance behaviour as predicted by FDTD simulations. In particular, we note that some of the multi-crystalline antennas remain completely dark (see e.g. the yellow-dashed circle in Fig. 4). Checking the



respective SEM images, it is found that all dark antennas have gaps that are not completely cut through, possibly due to the presence of a grain. It is further observed that overall the structural quality of single-crystalline antennas is significantly improved compared to the multi-crystalline counterparts. While many of the multi-crystalline antennas exhibit structural defects (see Fig. 4d, upper row), including defective gaps, the single-crystalline antennas very reproducibly display homogenous structural properties, such as width, gap, shape and relative orientation of the two antenna arms. In particular, the examples shown in Fig. 4 clearly illustrate our finding that dipole antennas fabricated from single-crystalline flakes reproducibly show the predicted length-dependent behaviour since the gap width can be kept constant over a whole array of structures. In contrast, for a multi-crystalline gold film without adhesion layer the gap width shows strong variations - only occasionally structures of high quality can be found.

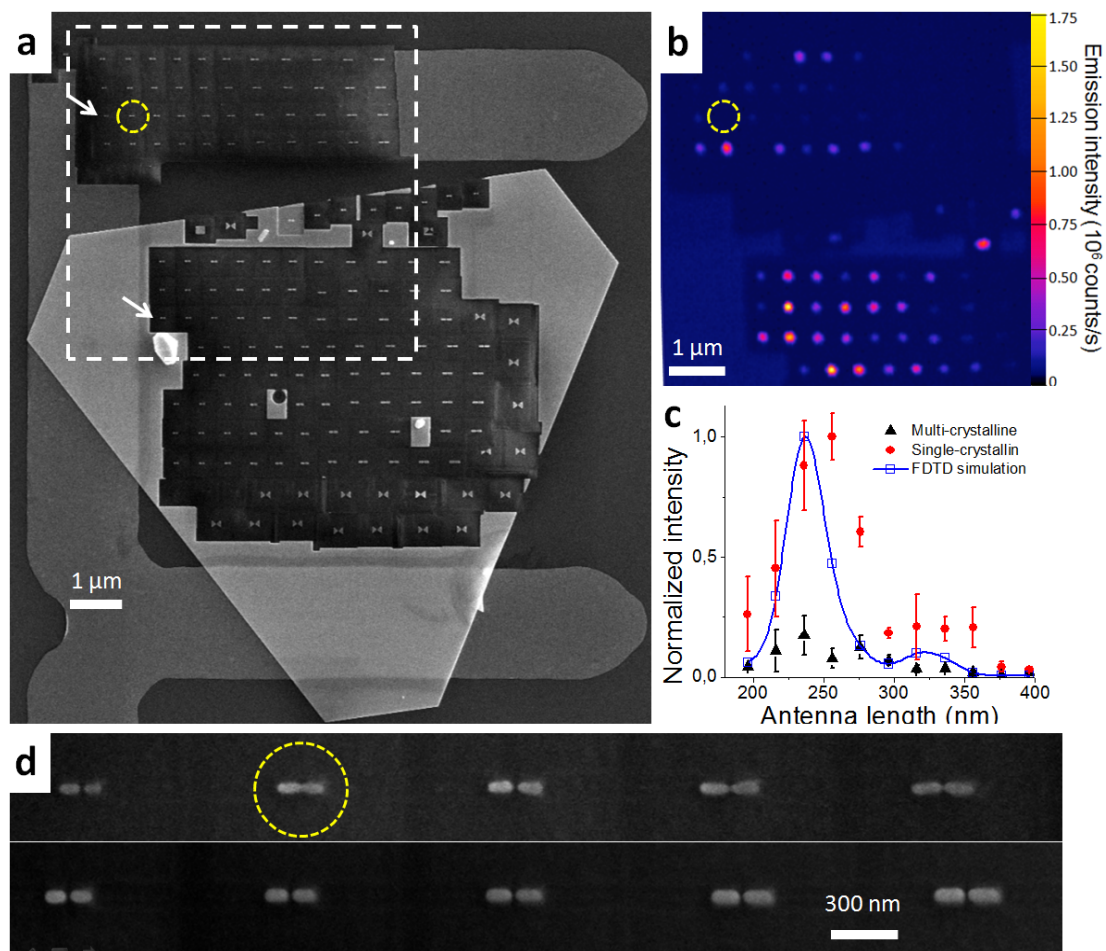


**Figure 4 | SEM image and corresponding TPPL map of single-crystalline and multi-crystalline linear dipole nanoantennas** (a) SEM overview image of the entire area subject to FIB milling showing a large single-crystalline gold flake and patches of a vapor-deposited multi-crystalline gold film without adhesion layer on top of a sputtered ITO substrate. (b) TPPL map of the area marked with the white-dashed rectangle in (a). (c) Averaged integrated TPPL intensity obtained from nanoantennas on single-crystalline (red dots) and multi-crystalline (black triangles) gold film in the white-dashed area in (a), plotted versus nominal antenna length together with results obtained from the simulation (blue open squares, blue solid line is a guide for the eye). All experimental results are normalized to the maximal signal obtained from single-crystalline nanoantennas and the error bars indicate the standard deviation. (d) Zoomed-in SEM images of the antenna series indicated by the white arrows in (a).

In conclusion we demonstrate a new method for the FIB fabrication of single-crystalline plasmonic nanostructures using large and thin, chemically grown single-crystalline gold flakes deposited onto a glass/ITO surface. This combination of bottom-up and top-down nanofabrication yields greatly improved fabrication tolerances as well as improved structural homogeneity as compared to conventional multi-crystalline structures. We are therefore able to fabricate plasmonic gold nanostructures with reproducible and well-defined nanometer scale features extending over micrometer length scales. We demonstrate the improved optical quality of our structures by means of the enhanced TPPL emission of single-crystalline linear dipole and bowtie optical antennas which serves as a benchmark for their strong near-field intensity enhancement. Our method opens the road for the fabrication and realization of high-definition complex plasmonic nanodevices and extended optical nanocircuits.

### **Acknowledgement**

The authors thank Prof. N. Gu and M. Mitterer for valuable discussions and assistance in the synthesis of gold flakes. We also thank S. Meier, T. Schmeiler and M. Emmerling for the assistance in FIB, AFM and EBL.

### **Author contributions**

B.H. conceived the original idea. J.S.H. and C.B. synthesized the gold flakes. J.S.H. and V.C. performed FIB and SEM. P.W. performed EBL. J.C.P. performed AFM. J.S.H., P.G. and J.K. carried out the optical experiments. J.S.H. designed and implemented numerical simulations; analyzed and assembled the data. J.S.H. and B.H. wrote the manuscript. All authors contributed to scientific discussions and critical revision of the article. M.K., A.F., U.S. and B.H. supervised the study.

### **Additional information**

Supplementary information accompanies this paper at [www.nature.com/nnano](http://www.nature.com/nnano). Reprints and permission information is available online at <http://npg.nature.com/reprintsandpermissions/>. Correspondence and requests for materials should be addressed to J.S.H. ([jhuang@physik.uni-wuerzburg.de](mailto:jhuang@physik.uni-wuerzburg.de)) and B.H. ([hecht@physik.uni-wuerzburg.de](mailto:hecht@physik.uni-wuerzburg.de))

### **References**

1. Ozbay, E. Plasmonics: Merging photonics and electronics at nanoscale dimensions. *Science* **311**, 189-193 (2006).
2. Schuller, J. A. *et al.* Plasmonics for extreme light concentration and manipulation. *Nature Mater.* **9**, 193-204 (2010).

3. Gramotnev, D. K. & Bozhevolnyi, S. I. Plasmonics beyond the diffraction limit. *Nature Photon.* **4**, 83-91 (2010).
4. Atwater, H. A. & Polman, A. Plasmonics for improved photovoltaic devices. *Nature Mater.* **9**, 205-213 (2010).
5. Bozhevolnyi, S. I., Volkov, V. S., Devaux, E., Laluet, J.-Y. & Ebbesen, T. W. Channel plasmon subwavelength waveguide components including interferometers and ring resonators. *Nature*, **440**, 508-511 (2006).
6. Oulton, R. F., Sorger, V. J., Genov, D. A., Pile, D. F. P. & Zhang, X. A hybrid plasmonic waveguide for subwavelength confinement and long-range propagation. *Nature Photon.* **2**, 496-500 (2008).
7. Mühlischlegel, P., Eisler, H.-J., Martin, O. J. F., Hecht, B. & Pohl, D. W. Resonant optical antennas. *Science* **308**, 1607-1609 (2005).
8. Kinkhabwala, A. *et al.* Large single-molecule fluorescence enhancements produced by a bowtie nanoantenna. *Nature Photon.* **3**, 654-657 (2009).
9. Pacifici, D., Lezec, H. J. & Atwater, H. All-optical modulation by plasmonic excitation of CdSe quantum dots. *Nature Photon.* **1**, 402-406 (2007).
10. Cai, W., White, J. S. & Brongersma, M. L. Compact, high-speed and power-efficient electrooptic plasmonic modulators. *Nano Lett.* **9**, 4403-4411 (2009).
11. Farahani, J. N., Pohl, D. W., Eisler, H.-J. & Hecht, B. Single quantum dot coupled to a scanning optical antenna: A tunable superemitter. *Phys. Rev. Lett.* **95**, 017402 (2005).
12. Anger, P., Bharadwaj, P. & Novotny, L. Enhancement and quenching of single-molecule fluorescence. *Phys. Rev. Lett.* **96**, 113002 (2006).
13. Kühn, S., Håkanson, U., Rogobete, L. & Sandoghdar, V. Enhancement of single-molecule fluorescence using a gold nanoparticle as an optical nanoantenna. *Phys. Rev. Lett.* **97**, 017402 (2006).
14. Weber-Bargioni, A. *et al.* Functional plasmonic antenna scanning probes fabricated by induced-deposition mask lithography. *Nanotechnol.* **21**, 065306 (2010).
15. Kim, S., Jin, J., Kim, Y.-J., Park, I.-Y., Kim, Y. & Kim, S.-W. High-harmonic generation by resonant plasmon field enhancement. *Nature* **453**, 757-760 (2008).
16. Hanke, T. *et al.* Efficient nonlinear light emission of single gold optical antennas driven by few-cycle near-infrared pulses. *Phys. Rev. Lett.* **103**, 257404 (2009).
17. Chang, D. E., Sørensen, A. S., Hemmer, P. R. & Lukin, M. D. Quantum optics with surface plasmons. *Phys. Rev. Lett.* **97**, 053002 (2006).
18. Akimov, A. V. *et al.* Generation of single optical plasmons in metallic nanowires coupled to quantum dots. *Nature* **450**, 402-406 (2007).
19. Chang, D. E., Sørensen, A. S., Demler, E. A. & Lukin, M. D. A single-photon transistor using nanoscale surface plasmons. *Nature Phys.* **3**, 807-812 (2007).
20. Kolesov, R. *et al.* Wave-particle duality of single surface plasmon polaritons. *Nature*

- Phys.* **5**, 470-474 (2009).
21. Aeschlimann, M. *et al.* Adaptive subwavelength control of nano-optical fields. *Nature*, **446**, 301-304 (2007).
  22. Huang, J. S., Voronine, D. V., Tuchscherer, P., Brixner, T. & Hecht, B. Deterministic spatiotemporal control of optical fields in nanoantennas and plasmonic circuits. *Phys. Rev. B* **79**, 195441 (2009).
  23. Tuchscherer, P. *et al.* Analytic coherent control of plasmon propagation in nanostructures. *Opt. Express* **17**, 14235-14259 (2009).
  24. Seidel, J., Grafström, S. & Eng, L. Stimulated emission of surface plasmons at the interface between a silver film and an optically pumped dye solution. *Phys. Rev. Lett.* **94**, 177401 (2005).
  25. Noginov, M. A., Zhu, G., Mayy, M., Ritzo, B. A., Noginova, N. & Podolskiy, V. A. Stimulated emission of surface plasmon polaritons. *Phys. Rev. Lett.* **101**, 226806 (2008).
  26. Noginov, M. A. *et al.* Demonstration of a spaser-based nanolaser. *Nature*, **460**, 1110-1113 (2009).
  27. Oulton, R. F. *et al.* Plasmon lasers at deep subwavelength scale. *Nature*, **461**, 629-632 (2009).
  28. Alù, A. & Engheta, N. Input impedance, nanocircuit loading, and radiation tuning of optical nanoantennas. *Phys. Rev. Lett.* **101**, 043901 (2008).
  29. Huang, J. S., Feichtner, T., Biagioni, P. & Hecht, B. Impedance matching and emission properties of nanoantennas in an optical nanocircuit. *Nano Lett.* **9**, 1897-1902 (2009).
  30. Chen, K.-P., Drachev, V. P., Borneman, J. D., Kildishev, A. V. & Shalaev, V. M. Drude relaxation rate in grained gold nanoantennas. *Nano Lett.* **10**, 916-922 (2010).
  31. Kuttge, M. *et al.* Loss mechanisms of surface plasmon polaritons on gold probed by cathodoluminescence imaging spectroscopy. *Appl. Phys. Lett.* **93**, 113110 (2008).
  32. Ditlbacher, H. *et al.* Silver nanowires as surface plasmon resonators. *Phys. Rev. Lett.* **95**, 257403 (2005).
  33. Callegari, V. Ph.D thesis, DISS. ETH Nr. 18558. DOI:10.3929/ethz-a-005933740
  34. Neff, N., Zong, W., Lima, A. M. N., Borre, M. & Holzhüter, G. Optical properties and instrumental performance of thin gold films near the surface plasmon resonance. *Thin Solid Films.* **496**, 688-697 (2006).
  35. Barchiesi, D. *et al.* Plasmonics: influence of the intermediate (or stick) layer on the efficiency of sensors. *Appl. Phys. B* **93**, 177-181 (2008).
  36. Aouani, H. *et al.* Crucial role of the adhesion layer on the plasmonic fluorescence enhancement. *ACS Nano* **3**, 2043-2048 (2009).
  37. Jiao, X., Goeckeritz, J., Blair, S. & Oldham, M. Localization of near-field resonances in bowtie antennae: Influence of adhesion layers. *Plasmonics* **4**, 37-50 (2009).
  38. Nagpal, P., Lindquist, N. C., Oh, S.-H. & Norris, D. J. Ultrasmooth patterned metals for

- plasmonics and metamaterials. *Science* **325**, 594-597 (2009).
39. Lofton, C. & Sigmund, W. Mechanisms controlling crystal habits of gold and silver colloids. *Adv. Funct. Mater.* **15**, 1197-1208 (2005).
  40. Guo, Z. *et al.* Facile synthesis of micrometer-sized gold nanoplates through an aniline-assisted route in ethylene glycol solution. *Colloids and Surfaces A: Physicochem. Eng. Aspects* **278**, 33-38 (2006).
  41. Millstone, J. E., Hurst, S. J., Métraux, G. S., Cutler, J. I. & Mirkin, C. A. Colloidal gold and silver triangular nanoprisms. *Small* **5**, 646-664 (2009).
  42. Beversluis, M. R., Bouhelier, A. & Novotny, L. Continuum generation from single gold nanostructures through near-field mediated intraband transitions. *Phys. Rev. B* **68**, 115433 (2003).
  43. Vesseur, E. J. R. *et al.* Surface plasmon polariton modes in a single-crystal Au nanoresonator fabricated using focused-ion-beam milling. *Appl. Phys. Lett.* **92**, 083110 (2008).
  44. Huang, J. S. *et al.* Mode imaging and selection in strongly coupled nanoantennas arXiv:1002.3887v1 (2010).
  45. Imura, K., Nagahara, T. & Okamoto, H. Plasmon mode imaging of single gold nanorods. *J. Am. Chem. Soc.* **126**, 12730-12731 (2004).
  46. Schnell, M. *et al.* Controlling the near-field oscillations of loaded plasmonic nanoantennas. *Nature Photon.* **3**, 287-291 (2009).

# Supplementary Information

## Atomically flat single-crystalline gold nanostructures for plasmonic nanocircuitry

Jer-Shing Huang<sup>1,\*</sup>, Victor Callegari<sup>3</sup>, Peter Geisler<sup>1</sup>, Christoph Brüning<sup>1</sup>, Johannes Kern<sup>1</sup>, Jord C. Prangma<sup>1</sup>, Pia Weinmann<sup>2</sup>, Martin Kamp<sup>2</sup>, Alfred Forchel<sup>2</sup>, Paolo Biagioni<sup>4</sup>, Urs Sennhauser<sup>3</sup>, Bert Hecht<sup>1,†</sup>

*1. Nano-Optics & Biophotonics Group, Experimentelle Physik 5, Physikalisches Institut, Wilhelm-Conrad-Röntgen-Center for Complex Material Systems, Universität Würzburg, Am Hubland, D-97074 Würzburg, Germany*

*2. Technische Physik, Physikalisches Institut, Wilhelm-Conrad-Röntgen-Center for Complex Material Systems, Universität Würzburg, Am Hubland, D-97074 Würzburg, Germany*

*3. EMPA, Swiss Federal Laboratories for Materials Testing and Research, Electronics/Metrology Laboratory, CH-8600 Dübendorf, Switzerland*

*4. CNISM - Dipartimento di Fisica, Politecnico di Milano, Piazza Leonardo da Vinci 32, 20133 Milano, Italy*

\* jhuang@physik.uni-wuerzburg.de

† hecht@physik.uni-wuerzburg.de

## 1. Preparation and characterization of self-assembled single-crystalline gold microflakes

Single-crystalline gold flakes are prepared following the procedure described in ref. 40. The flake suspension is sonicated for 5 minutes right before being drop-casted on the ITO glass substrate. After the solvent dries out, flakes with sufficiently large area and homogeneous contact with the substrate are pre-selected using wide-field optical microscope with a low-magnification air objective (20x). The sample is then transferred into the vacuum chamber for SEM and FIB milling. Pre-selected flakes are double checked with SEM, where the homogeneity of image brightness is used as a positive indicator. Multi-crystalline structures are fabricated on EBL fabricated marker structures nearby the selected flakes to ensure identical local environment and identical FIB focusing conditions. All the structures in this work are milled with Ga-ions using an acceleration voltage of 30 kV and a typical current of 1.5 pA. Although the same FIB patterns are used to fabricate the structures, the ion-beam dose is optimized for the multi-crystalline and single-crystalline areas, respectively, so that the finest features, e.g. the gap size of the nanoantennas or the width of a linear cut, were comparable. Fig. S1 shows the SEM image of the area of interest including flake and marker structure (letter F) before and after FIB milling.

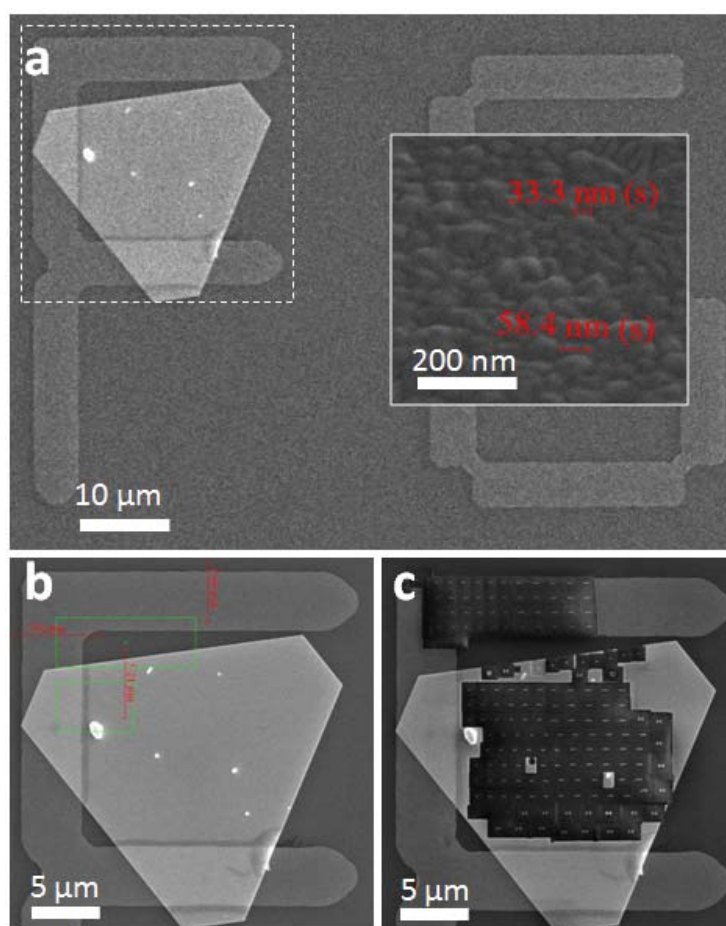


**Figure S1 | SEM image of an area containing chemically synthesized single- and vapor-deposited multi-crystalline gold films.** (a) Overview of the area of interest including both parts of the multi-crystalline marker structure and the single-crystalline flake. The inset shows a zoomed-in image of the typical surface of vapor-deposited multi-crystalline gold film consisting of randomly orientated



grains. (b) Zoomed-in SEM image of the dashed area in (a) before FIB milling. (c) Same area after FIB milling.

In order to maximize the size of the flakes and therefore the area available for FIB milling, we have decreased the temperature of the chemical reaction to 60°C and increased the reaction time to more than 12 hours. Figure S2 shows a histogram illustrating the temperature dependence of the flake size as obtained by evaluating optical images of flakes deposited on substrates as described above. While the average flake size increases with decreasing reaction temperature, the average flake thickness remains smaller than 80 nm which facilitates the fabrication.

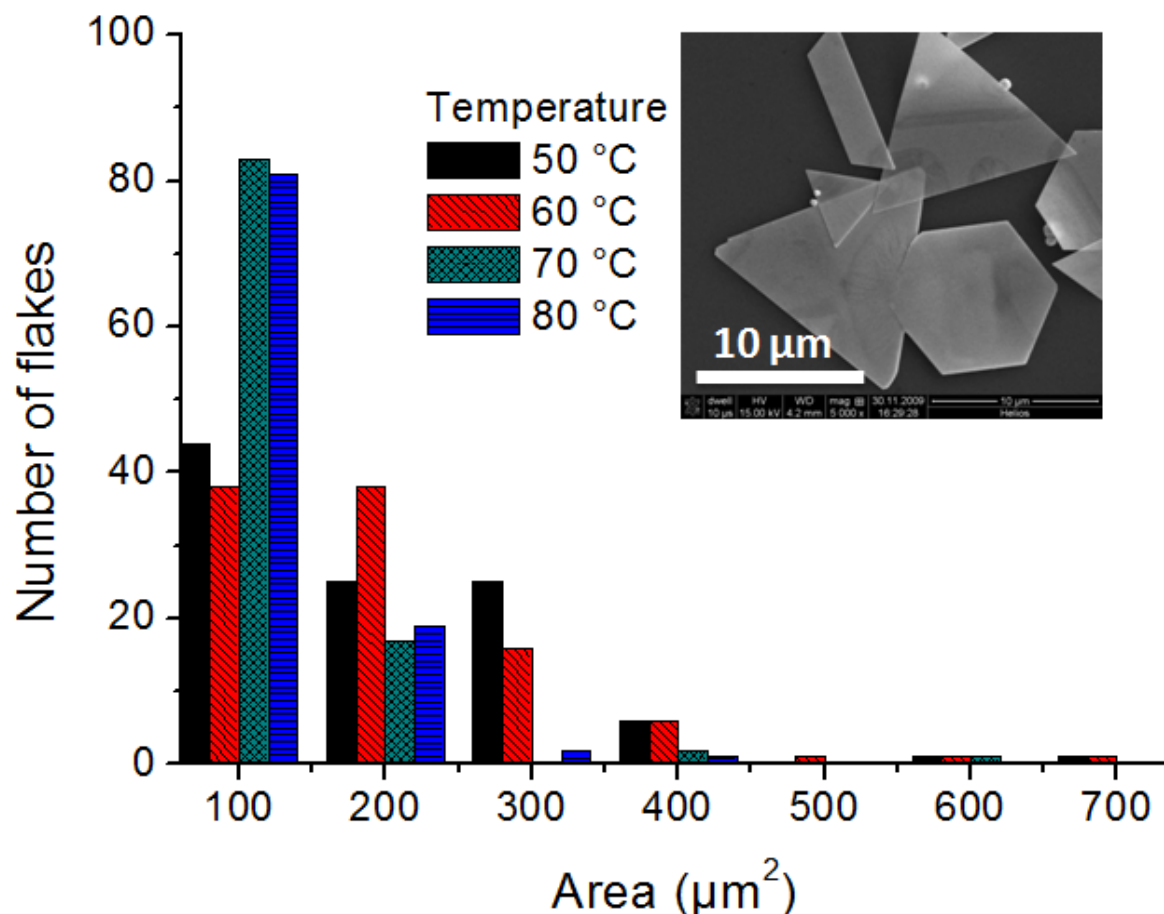


**Figure S2 | Flake area distribution with respect to the reaction temperature.** The histogram is obtained by measuring the area of 100 randomly sampled flakes from each sample suspension. The mostly commonly encountered shapes of the flakes are triangles and truncated triangles as shown in the inset.

We have performed atomic force microscopy (AFM) and confirm that the surface roughness of the flake is smaller than 1 nm over an area of 1 μm<sup>2</sup>. A typical AFM image with corresponding topography histogram is shown in Fig. S3. The fluctuation of the surface height is mainly due to the surfactant and other contaminations from the solvent. In addition, extremely low yield of visible two-photon photoluminescence (TPPL) signal from the single-crystalline flakes can also serve as an evidence for the ultrasmooth flake surface. As shown in Fig. S4, even for 500 μW focused excitation (830 nm, 1 ps, N.A.=1.4), the flat flake shows no significant spectrally dispersed TPPL as compared to the multi-crystalline marker area and nanoantennas, which is in agreement with previous studies [refs. 42, S1].

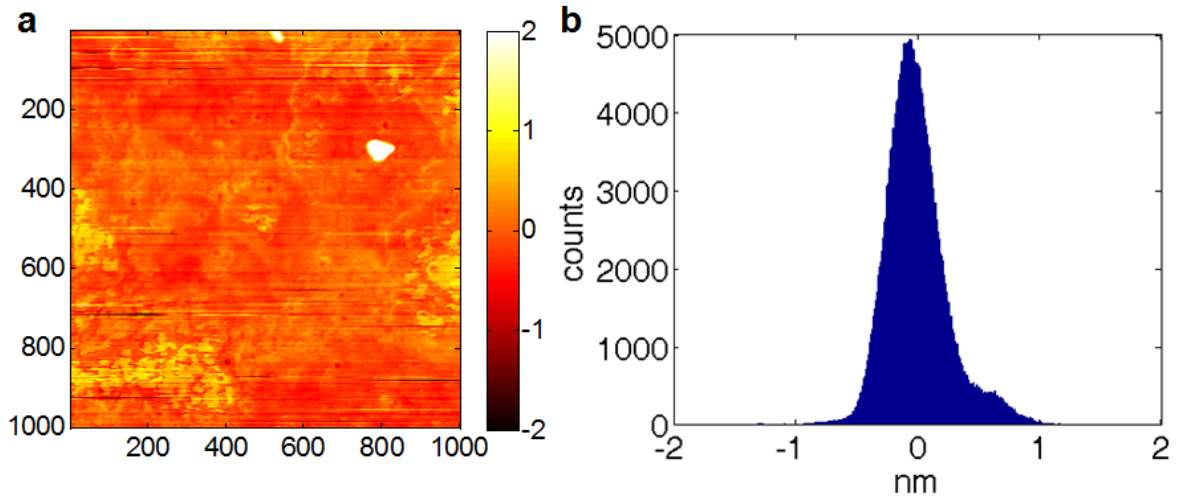


**Figure S3 | AFM images of a single-crystalline flake surface.** (a) Typical AFM image of the surface topography of a single-crystalline flake. (b) Distribution of the surface height over a  $1 \mu\text{m}^2$  area. The surface roughness is smaller than 1 nm.

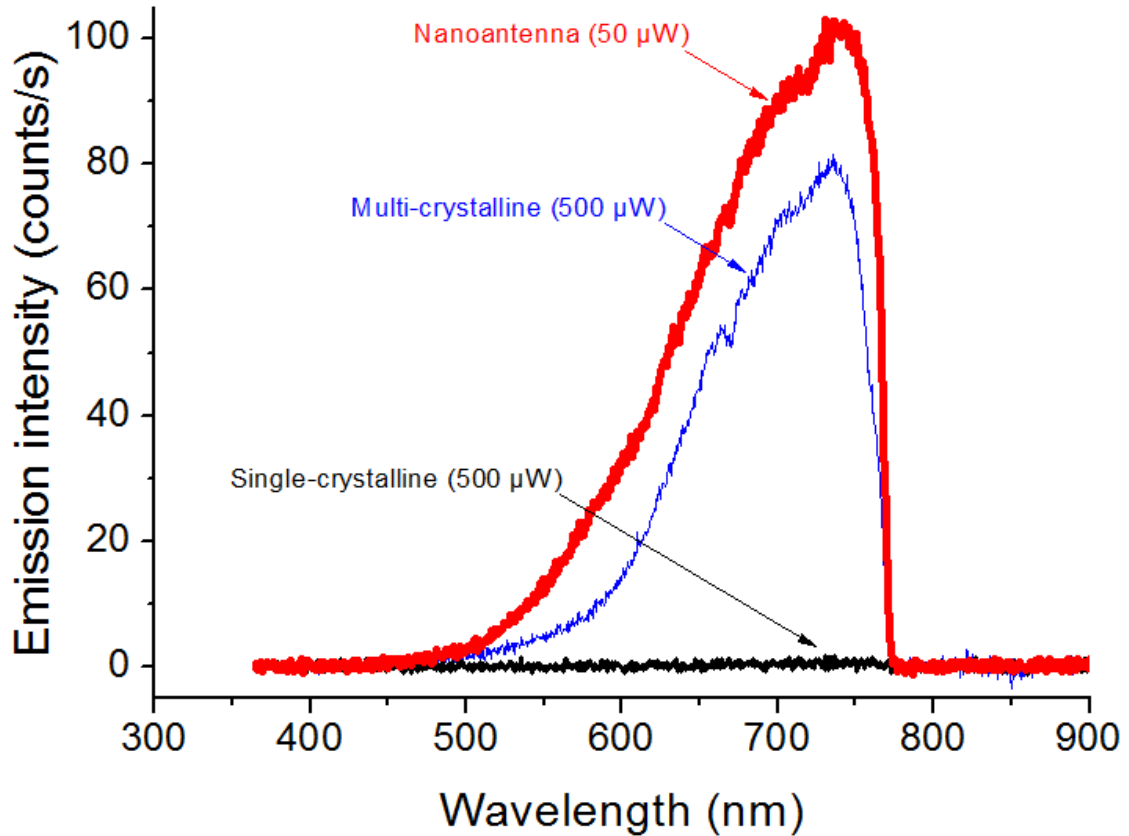


**Figure S4 | Two-photon photoluminescence (TPPL) spectra of a resonant nanoantenna as well as single- and multi-crystalline gold films.** Due to the surface roughness, unstructured multi-crystalline gold marker (blue thin line) exhibits much stronger TPPL signal compared to the unstructured single-crystalline flake (black medium line). However, when the single-crystalline gold film is shaped into a resonance linear dipole nanoantenna (50 nm wide, 30 nm high and 236 nm long with 16 nm feedgap, red thick line), the TPPL signal is greatly enhanced. Note that the excitation polarization for the nanoantenna curve is along the antenna long axis and the excitation power is 50  $\mu\text{W}$  (830 nm, 1 ps, N.A.=1.4).

## 2. Two-photon photoluminescence confocal microscopy

The distance between adjacent antennas is larger than 700 nm to minimize crosstalk and to ensure that only one antenna is illuminated by the focal spot (FWHM = 350 nm). The ultrashort pulses from a mode-locked Ti:sapphire laser (center wavelength = 828 nm, 80 fs, 80 MHz, average power: 50 - 500  $\mu$ W, Time-Bandwidth Products, Tiger) are coupled into 1.5 m of optical fiber to get stretched to 1 ps, which avoids possible damage of the nanoantennas without decreasing the TPPL signal. The linear polarized fiber output is then collimated, passes a dichroic mirror (DCXR770, Chroma Technology Inc.) and is focused through the cover glass onto the antenna array using an oil immersion microscope objective (Plan-APO 100x, Oil, NA = 1.4, Nikon). The direction of linear polarization of the beam is adjusted using a  $\lambda/2$ -plate. The photoluminescence signal is collected by the same objective and is reflected by the dichroic mirror. Laser scattering and possible second harmonic signals are rejected by a holographic notch filter (O.D. > 6.0 at 830 nm, Kaiser Optical System, Inc.) and a bandpass filter (transmission window: 450-750 nm, D600/300, Chroma Technology Inc.) in front of the photon detector (SPCM-AQR 14, Perkin-Elmer). A typical emission spectrum of a resonant nanoantenna is shown in Fig. S4. The quadratic dependence of the recorded integrated signal on the excitation power confirms that the visible TPPL of gold dominates the antenna emission (Fig. S5). Figure S6 shows the dependence of the TPPL signal intensity on the excitation polarization which verifies that the longitudinal antenna resonance is excited.

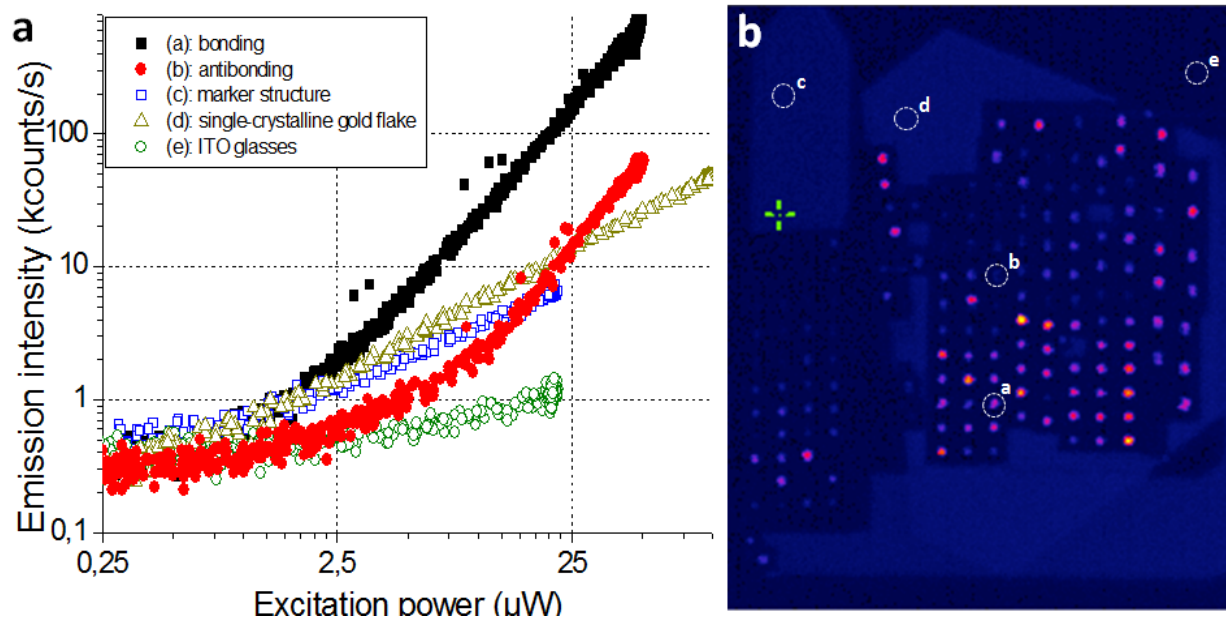


**Figure S5 | Intensity dependence of visible TPPL signals on the average excitation power** (a) Emission intensity as a function of the excitation power obtained from the areas marked with the dashed circles in the emission map (b). The emission signals from antennas with bonding (black solid squares) and antibonding (red solid dots) resonance show quadratic dependence on the excitation power while the scattering from the multi-crystalline gold marker structure (blue open square), single-crystalline gold flake (yellow open triangle) and bare ITO glass area (green open circle) show very weak scattering with linear dependence on the excitation power.

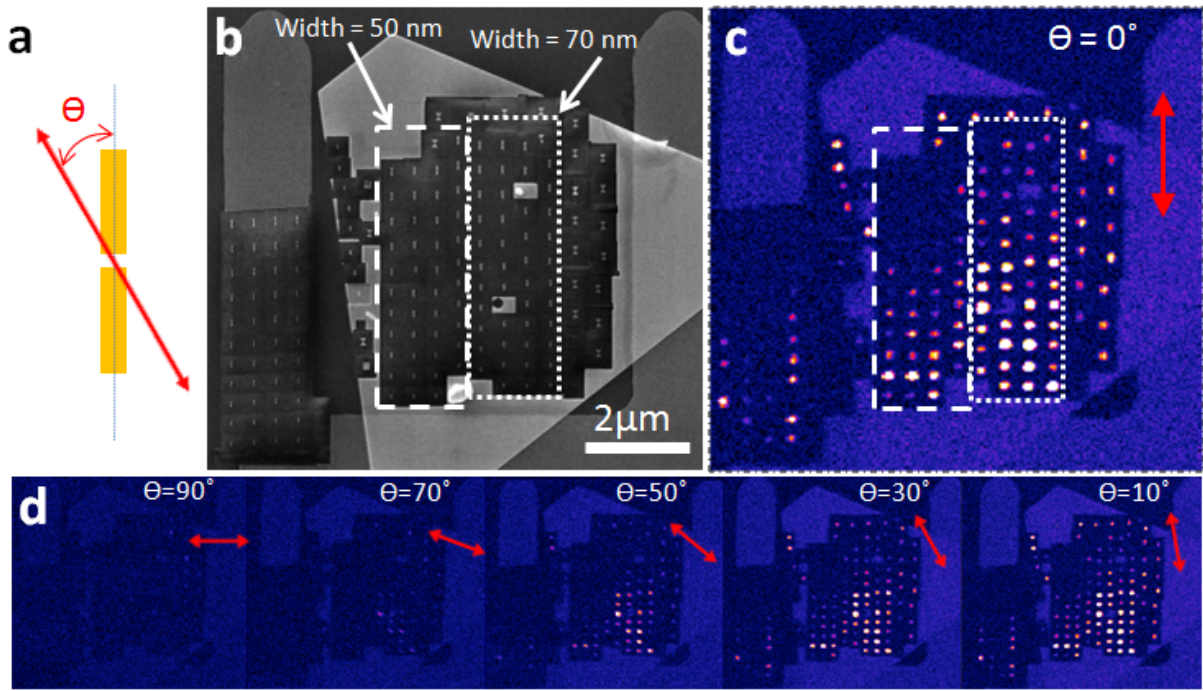


**Figure S6 | SEM image and TPPL maps of the whole antenna array obtained with different excitation polarizations.** (a) Schematic diagram of the linear excitation polarization (red double arrows).  $\Theta$  is defined as the angle between the excitation polarization and the antenna's long axis; (b) SEM image of the fabricated area including arrays of antennas with nominal width of 50 nm (dashed rectangle) and 70 nm (dotted rectangle) ; (c) TPPL map of the corresponding area shown in (b) with longitudinal excitation ( $\Theta = 0^\circ$ ); (d) TPPL maps for various excitation polarizations. Same intensity scale for all TPPL maps. Note that these images are rotated counterclockwise by  $90^\circ$  as compared to Fig. 4.

### 3. Numerical simulations

The resonance of the fabricated bowtie nanoantennas in Fig. 2 is simulated using the nominal dimensions used in the FIB milling. The gold bowtie nanoantennas are placed on top of an ITO layer. Since the antenna response is sensitive to the local index of refraction, also the geometry changes of the substrate due to the FIB milling are taken into account. Figure S7a-c shows the top view and cross section of the simulated structure. The dielectric function of gold is described by an analytical model [ref. S2] which fits the experimental data [ref. S3], while the dielectric function of the sputtered ITO layer is based on experimental data [ref. S4]. A multi-coefficient model [ref. S5] is then used to fit the dielectric function within the frequency window of interest to gain speed in the simulation. A uniform mesh volume with discretization of  $1 \text{ nm}^3$  covers the whole antenna and all the boundaries of the simulation box are set to be at least 700 nm away from the antenna to avoid spurious absorption of the antenna near fields. Corners of the antenna arms are rounded in the simulations using cylinders with 10 nm diameter. The source is set to have the same spectral width as the laser used in the experiment (821 - 835 nm) and is focused onto the gold/ITO interface at the feedgap center using a thin lens (N.A. = 1.4) focusing approximated by a superposition of 200 plane waves. The impulse spectrum is recorded at the center of the feedgap and normalized to the source spectrum. Figure S7d shows the simulated spectra of the bowtie nanoantenna sketched in Fig. S7a-c,



in which the laser spectrum used in the experiments indicated by the shaded area overlaps only partially with the resonance. Slightly different spectra are obtained for different microscopic conditions at the feedgap as indicated in Fig. S7d.

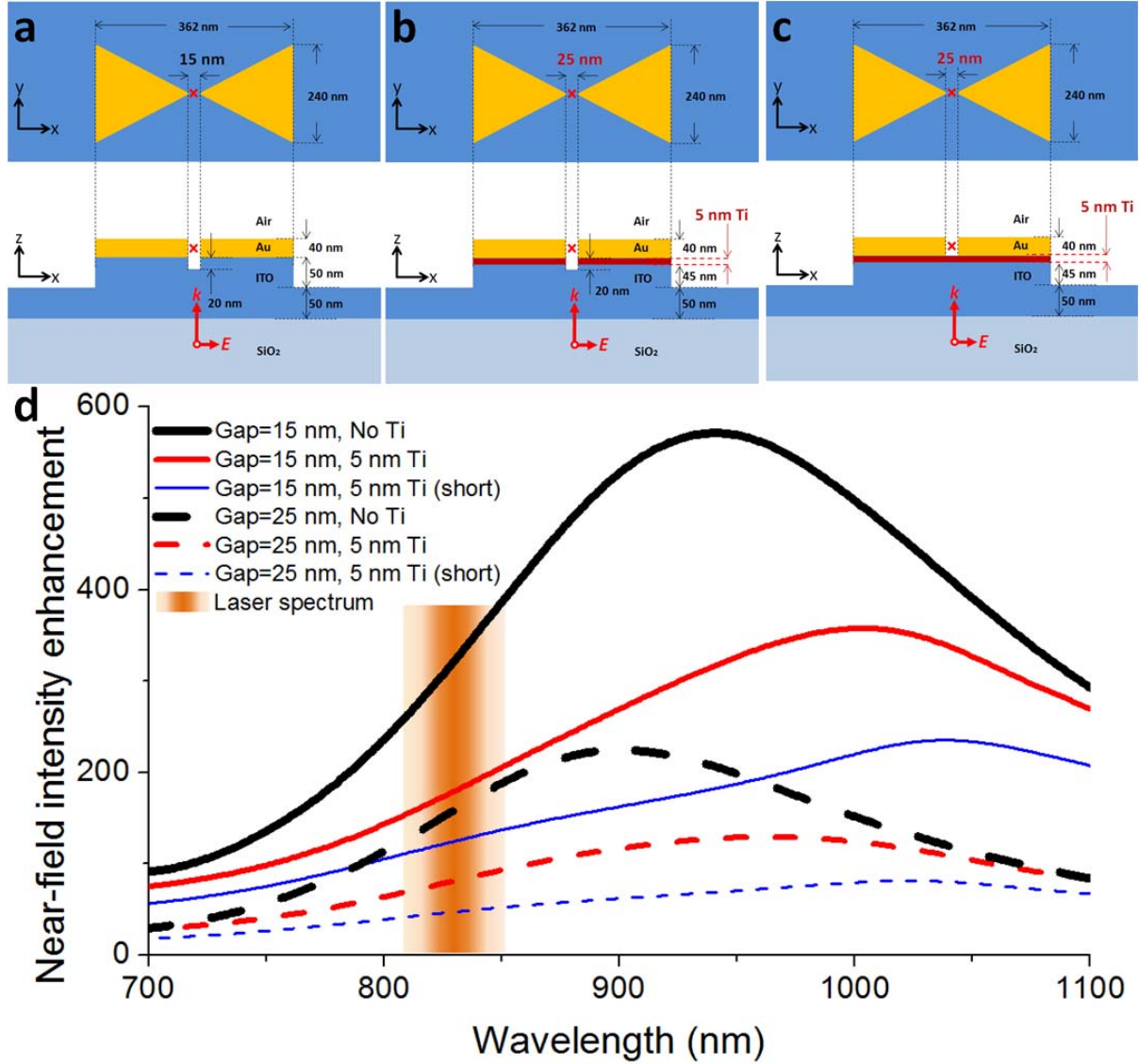


**Figure S7 | Schematic diagram of the simulated structures and the impulse spectra** (a) Top view and cross section of a gold bowtie antenna with (a) 15nm gap on ITO substrate, (b) a 25 nm gap and 5 nm Ti adhesion layer between gold and ITO substrate cut through in the gap and (c) a 25 nm gap and 5 nm Ti adhesion layer between gold and ITO substrate not cut through in the gap. The excitation source (symbolized by the red arrows) is focused onto the feedgap center. Near-field intensity spectra are recorded at the feed gap center (red crosses). (d) The simulated spectra of the bowtie nanoantennas sketched in (a)-(c). The shaded area indicates the real source spectral range, which does not hit the resonance peak but partially overlaps with the broad resonance peak.

## Supplementary Reference

- S1. Boyd, G. T., Yu, Z. H. & Shen, Y. R. Photoinduced Luminescence from the noble metals and its enhancement on roughened surface. *Phys. Rev. B* **33**, 7923-7936 (1986).
- S2. Etchegoin, P. G., le Ru, E. C. & Meyer M. An analytic model for the optical properties of gold. *J. Chem. Phys.* **125**, 164705 (2006).
- S3. Johnson, P. B. & Christy, R. W. Optical constants of noble metals. *Phys. Rev. B* **6**, 4370 (1972).
- S4. Laux, S. *et al.* Room-temperature deposition of indium tin oxide thin films with plasma ion-assisted evaporation. *Thin Solid Films* **335**, 1-5 (1998).
- S5. [http://www.lumerical.com/fdtd\\_multicoefficient\\_material\\_modeling.php](http://www.lumerical.com/fdtd_multicoefficient_material_modeling.php)